The Influence of Air Void Content on Moisture Damage Susceptibility of Asphalt Mixtures: A Computational Study

A. Varveri[1], S. Avgerinopoulos[2], C. Kasbergen[1], A. Scarpas[1] and A. Collop[2]

[1]Section of Road Engineering
Faculty of Civil Engineering & Geosciences
Delft University of Technology
Address: Stevinweg 1, 2628 CN, Delft, The Netherlands.
Tel: +31152784665, Fax: +31152785767, Email: a.varveri@tudelft.nl

[2]Department of Engineering
Faculty of Technology
De Montfort University
Address: The Gateway, LE1 9BH, Leicester, United Kingdom
Tel: +44 116 257 7092, Fax: +44 116 250 6092, Email: savgerinopoulos@dmu.ac.uk

Total Number of Words

Number of words in text:	=	4112	words
Number of tables: (1x250)	=	250	words equivalent
Number of figures: (9x250)	=	2250	words equivalent
---			---
Total number of words	=	6612	words equivalent

Date of paper submission: 1 March 2014

Corresponding author:
A. Varveri
Section of Road Engineering
Faculty of Civil Engineering & Geosciences
Delft University of Technology
Address: Stevinweg 1, 2628 CN, Delft, The Netherlands.
Tel: +31152784665, Fax: +31152785767, Email: a.varveri@tudelft.nl

ABSTRACT

Because of the difficulties associated with the generation of finite element meshes based on X-Ray Computed Tomography scans and the extraordinary computational demands in performing 3D finite element analyses, past modelling efforts have focused primarily on 2D representations of asphalt mixtures and have placed no emphasis on the inclusion of the air voids network within the body of an asphalt concrete specimen. A 3D micromechanical moisture damage model has been developed and implemented in the finite element system CAPA-3D capable of addressing individually the three main phases of asphalt concrete: aggregate, mastic and air voids. 3D finite element meshes of different types of asphalt mixtures were generated on the basis of X-Ray scans. By means of CAPA-3D the significance of the air voids structure in the development of moisture damage in asphalt concrete specimens was demonstrated. Availability of the model enables evaluation and ranking of the contribution of the characteristics of the individual mixture components to the overall mixture moisture resistance.

INTRODUCTION

Moisture damage has been identified as a major contributor to accelerated deterioration in asphalt concrete (AC) pavements. At micromechanical level, moisture-induced damage is described as the loss of strength and durability of the asphalt mixture through loss of adhesion between the asphalt binder and the aggregates, as well as through loss of cohesive resistance of the asphalt binder itself *(1)*. Moisture diffusion, desorption of the asphalt binder due to fast water flows and cyclic pore pressure development from entrapped water in the air voids (i.e. pumping action) were identified as the physical and/or mechanical processes that ultimately can lead to pavement distresses *(2,3)*. In the majority of cases, moisture diffusion is the primary cause of mixture degradation; depending on circumstances, the effects of the other processes accentuate the phenomenon.

Moisture diffusion in asphalt mixtures is a long-term process *(4)* driven by the diffusion characteristics of each type of asphalt binder. As moisture diffuses into the mixture, the properties of the binder change causing a decrease in the cohesive strength and consequently an overall reduction in the stiffness and strength of the pavement. Additionally, in the presence of moisture, the adhesive bond characteristics between the aggregate and the binder change in time and the integrity of the bond diminishes, hence resulting in stripping of the aggregates from the asphalt mixture *(5-8)*.

Several models have been proposed for the simulation of moisture diffusion induced damage over the past years *(9-13)*. Even though many researchers have discussed the influence of air voids on moisture damage *(14-17)*, in all modelling efforts presented so far AC has been simulated as a two-phase material (aggregates and mastic) and 2D representations of the internal structure of the samples were used. Because the behavior of multiphase materials, such as AC, is determined by the contribution and the interaction of the constituent materials as well as by their morphological and geometrical characteristics, the inclusion of air voids in finite element simulations is of paramount importance. Especially since, as in the case of moisture diffusion, air voids facilitate the ingress of moisture to the mastic and eventually to the aggregate-mastic interface.

In the present study, a coupled moisture-mechanical damage model is presented and the importance of the air void phase in the numerical simulation of moisture damage is demonstrated. All simulations were performed on 3D micromechanical meshes obtained via X-ray Computed Tomography (CT) scans of cores of various AC types. The constitutive model was implemented into the CAPA-3D Finite Element (FE) system developed at Delft University of Technology *(18)*.

COUPLED MECHANICAL-MOISTURE DAMAGE MODEL

An energy-based constitutive model for the simulation of coupled mechanical-moisture damage is presented in this section. The model falls within the general framework of Continuum Damage Mechanics (CDM) and introduces material damage as an internal state variable, which represents the irreversible physical processes within the microstructure of the material.

To include the notion of material damage into a large deformation viscoelastic framework, the following multiplicative decomposition of the deformation gradient tensor F is proposed, Figure 1.

$$F = F_{\infty} F_{d} \tag{1}$$

where F is the total deformation gradient, F_d is the damage deformation gradient and F_{∞} is the undamaged elastic deformation gradient. Furthermore, it is postulated that the undamaged rheological response is due to the contribution of an elastic and a viscoelastic component such that

$$F_{\infty} = F_e F_v \tag{2}$$

where F_v and F_e are the viscous and the elastic deformation gradients of the viscoelastic component.

With regard to the reference undamaged configuration, the right Cauchy-Green strain tensors C_∞ and C_e , for the deformation components F_∞ and F_e respectively, are described by:

$$C_\infty = F_\infty{}^T F_\infty \tag{3}$$

$$C_e = F_e{}^T F_e \tag{4}$$

where $F_\infty{}^T$ and $F_e{}^T$ are the transpose of the deformation tensors F_∞ and F_e . For a purely mechanical case (thermal effects are ignored), the Clausius-Planck dissipation inequality, or second law of thermodynamics, defines the dissipation of energy D , as

$$D = P : \dot{F} - \dot{\Psi} \geq 0 \tag{5}$$

where P is the first Piola-Kirchhoff stress, Ψ is the Helmholtz strain energy function and the dot indicates the time derivative. For the proposed model the Helmholtz free energy is defined as

$$\Psi = \Psi_v\left(C_e\right) + \Psi_\infty\left(C_\infty, d\right) \tag{6}$$

in which Ψ_v is the strain energy function of the visco-elastic component, Ψ_∞ is the strain energy function of the elastic component and d is damage. Substituting Eq. (6) into the dissipation inequality of Eq. (5) gives

$$D = P : \dot{F} - \frac{\partial \Psi_v}{\partial C_e} : \dot{C}_e - \frac{\partial \Psi_\infty}{\partial C_\infty} : \dot{C}_\infty - \frac{\partial \Psi_\infty}{\partial d} \cdot \dot{d} \geq 0 \tag{7}$$

Defining the time derivatives of the deformation tensors C_∞ and C_e , and rearranging the terms, the following equation can be obtained

$$\begin{aligned} D = &\left(P - \left(2F_e \frac{\partial \Psi_v}{\partial C_e} F_e^{-T} + 2F_\infty \frac{\partial \Psi_\infty}{\partial C_\infty} F_\infty^{-T} \right) F^{-T} \right) : \dot{F} + 2C_e \frac{\partial \Psi_v}{\partial C_e} : \dot{F}_v F_v^{-1} + \\ &+ C_\infty \left(2\frac{\partial \Psi_\infty}{\partial C_\infty} + 2F_v^{-1} \frac{\partial \Psi_v}{\partial C_e} F_v^{-T} \right) : \dot{F}_d F_d^{-1} - \frac{\partial \Psi_\infty}{\partial d} \cdot \dot{d} \geq 0 \end{aligned} \tag{8}$$

By standard arguments *(19)*, based on Eq. (8), the first Kirchhoff-Piola tensor P can be obtained

$$P = \left(2F_e \frac{\partial \Psi_v}{\partial C_e} F_e^{-T} + 2F_\infty \frac{\partial \Psi_\infty}{\partial C_\infty} F_\infty^{-T} \right) F^{-T} = \tau F^{-T} \tag{9}$$

where τ is the Kirchhoff stress. In addition, it should hold that

$$2C_e \frac{\partial \Psi_v}{\partial C_e} : \dot{F}_v F_v^{-1} + C_\infty \left(2\frac{\partial \Psi_\infty}{\partial C_\infty} + 2F_v^{-1} \frac{\partial \Psi_v}{\partial C_e} F_v^{-T} \right) : \dot{F}_d F_d^{-1} - \frac{\partial \Psi_\infty}{\partial d} \cdot \dot{d} \geq 0 \tag{10}$$

The above inequality can be further elaborated as

$$\Sigma_e : L_v + \overline{\Sigma} : L_d + q \cdot \dot{d} \geq 0 \quad , \quad q = -\frac{\partial \Psi_\infty}{\partial d} \tag{11}$$

where Σ_e and $\overline{\Sigma}$ are the Mandel stress tensor of the viscoelastic component and of the damage component respectively, q is the stress component due to damage and L_v and L_d are the corresponding viscous and damage velocity gradients. To solve the inequality defined in the above, the following minimization problem is defined

$$\text{minimize} \qquad -\left(\Sigma_e : L_v + \overline{\Sigma} : L_d + q \cdot \dot{d}\right) \tag{12}$$

$$\text{subject to} \qquad g\left(\overline{\Sigma}, q\right) \leq 0 \tag{13}$$

To satisfy the above minimization problem, the following evolution laws are postulated

$$L_v = \dot{F}_v F_v^{-1} = C_v^{-1} : \Sigma_e$$
$$L_d = \dot{F}_d F_d^{-1} = \mu \frac{\partial g}{\partial \bar{\Sigma}} \qquad \dot{d} = \mu \frac{\partial g}{\partial q} \tag{14}$$
$$\mu \geq 0, \quad g(\bar{\Sigma}, q) = h\left(\bar{\Sigma}\right) - \left(1-d\right)\left(h_y - q\right) \leq 0, \quad \mu g(\bar{\Sigma}, q) = 0$$

where $g(\bar{\Sigma}, q)$ is the damage flow surface, C_v^{-1} is a symmetric fourth order tensor representing viscosity, μ is the damage consistency parameter (similar to plasticity), h is a function of $\bar{\Sigma}$ and h_y is the stress 'yield' limit.

In this implementation, damage is a scalar quantity which can vary from the undamaged state $(d = 0)$ to the fully damaged one $(d = 1)$. Total damage is a combination of moisture induced damage and damage due to mechanical loading. The evolution law for the mechanical damage d_m is a function of the total dissipated viscous work W in the viscoelastic component and is described by

$$d_m = 1 - e^{-k \cdot W^r} \tag{15}$$

where k and r are damage related parameters. Similarly, moisture damage is a function of moisture content at various times *(10)* and is described as

$$d_\theta = 1 - e^{-a\sqrt{\theta}} \tag{16}$$

where α is the moisture damage susceptibility parameter and θ is the normalized concentration in the material at any given time. The moisture damage curves were fitted in experimental data obtained from a study by Kringos et al. *(20)*. The coupled mechanical-moisture damage function is further defined as

$$d = 1 - (1 - d_m)(1 - d_\theta) \tag{17}$$

DEVELOPMENT OF 3D MICROMECHANICAL MESHES

The accurate representation of the internal structure of the asphalt specimens is quite significant in micromechanical modeling, since each mixture component has its particular moisture diffusion characteristics and mechanical properties, and therefore the geometry of every single phase plays an important role on the propagation of moisture and the mechanical response of the asphalt mixture. In order to address this issue, in this study, three dimensional micromechanical FE meshes were produced from X-Ray CT scans by means of Simpleware, specialized 3D-based image processing software *(21)*.

In Figure 2, the typical process for the generation of 3D voxel-based FE meshes is presented schematically. In general, the process includes data preparation and filtering, segmentation of the individual masks, mask filtering and mesh generation.

In this study, FE meshes obtained from a stone mastic asphalt (SMA) and a porous asphalt (PA) mixture were used, Figure 3. Asphalt concrete slabs for both mixtures were prepared in the laboratory using a roller compactor and specimens of 60 mm in height and 100 mm in diameter were cored out of the slabs and used for X-Ray CT scanning. The SMA and PA mixtures had a nominal maximum aggregate size of 10 mm; the particle size distribution for both mixtures is given in Table 1. The binder content (P_b) and the air void percentage (AV) were 6.4 and 4.4 for the SMA; for the PA mixture P_b was 5.3 and AV was 23.7%.

Apart from air voids content, connectivity of the pores is also critical in determining the susceptibility of asphalt mixtures to moisture damage. From statistical analysis performed in both meshes, it has been found that pore connectivity reached almost 90% (of the total volume of the air void phase) for the PA mixture, Figure 3(c). Unlike the porous mixture, pore connectivity of the

dense mixture was quite low; only 10% of the pores were interconnected and the rest of the pore phase was divided in volume fractions of less than 2% each, Figure 3(d).

After cropping the segmented data to the desired dimensions, a robust meshing algorithm was applied to enable the conversion of the 2D images into FE meshes, that were used for computational analyses via the CAPA-3D FE system. For the analyses, both meshes were discretized by using 3D linear four-node tetrahedral elements. Specifically, the SMA mesh consists of 3,645,835 elements and the PA mesh consists of 2,223,084 elements. It is clear that when such detailed micromechanical meshes are employed for analyses, the computation time increases dramatically and the use of parallel computing resources is essential.

MICROMECHANICAL FINITE ELEMENT SIMULATIONS

The micromechanical model described in the above was utilized to perform finite element simulations of damage due to mechanical and moisture loading. Two types of asphalt mixtures (PA and SMA) were used with different mixture characteristics in terms of aggregate size and gradation, bitumen content, air void percentage and connectivity etc. The material properties of the constituents for both asphalt mixtures were identical, allowing thus the investigation of the influence of the different mixture composition characteristics on the total material response. Because of the different time scales associated with moisture diffusion and mechanical damage, a staggered computational procedure was implemented: moisture diffusion simulations were performed to generate the moisture concentration profiles within the asphalt specimens and then mechanical loading was applied.

Moisture diffusion through the asphalt mixture components is considered to be a process that occurs at molecular level. In the CAPA-3D finite element system, moisture diffusion is assumed to follow Fick's second law described by the following equation:

$$\frac{\partial \theta}{\partial t} = \nabla \left(D \nabla \theta \right) \tag{18}$$

where $0 \le \theta \le 1$ is the normalized moisture concentration in the material at any given time t, $\nabla \theta$ is the gradient of the normalized moisture concentration and D is the moisture diffusion coefficient. For both asphalt mixtures, moisture was allowed to infiltrate into the three-phase material system for different time intervals, in order to capture the effect of moisture concentration on the degradation of the mechanical properties of the mixtures. During the simulations, a constant moisture boundary condition was applied on the top and the sides of the asphalt specimen, thus simulating conditioning of specimens in a water bath in the laboratory.

In previous work, Kringos et al. *(22)* have determined the moisture diffusion coefficients of four mastic types and two aggregates types. Based on that work, the diffusion coefficients for the mastic and the aggregates were assumed 11.08×10^{-3} and 0.72 mm^2/hr, respectively. The diffusion coefficient of the air void phase was assumed 93.6×10^{3} mm^2/hr, value reported in the study of Kassem et al. *(15)*.

The normalized moisture concentration profiles, along the diameter of the PA and the SMA specimens at different time intervals, are shown in Figures 4 and 5, respectively. For the presentation of the results, a number of nodes were selected as output locations for the moisture concentration values. All the selected nodes are lying on the diameter of the specimens and are located 1 mm above the bottom surface of the samples.

The results from the moisture diffusion simulations clearly show the effect of air voids content and their connectivity, on the amount of moisture that is present in an asphalt specimen at any given time. After 120 hrs (5 days) of diffusion and for the same diffusivity properties of all constituent components, it can be seen from the above graphs that the PA specimen has greater values of moisture concentration compared to the SMA, because of its higher total air voids content and the greater diffusion rates associated with the air void phase.

In addition, it can be observed that the moisture profile for the PA mixture is more homogenized than for the SMA due to the high percentage of interconnected pores that allows moisture to diffuse in a uniform way through the body of the PA specimen. The generated moisture profiles, Figures 4-5, can be justified if the air voids characteristics of the specimens are taken into account. In Figure 3(c), the air void distribution of the PA specimen is illustrated. In blue color, the interconnected voids are shown, whereas the isolated air voids are in different colors. It can be observed that the peak shown in the graph for the PA mixture, Figure 4, coincides spatially with the presence of isolated voids in the specimen. This discontinuity in the air void network is a hindrance to the diffusion of moisture in that specific location of the sample. The same observations can be made for the SMA mixture, where the percentage of isolated voids is higher; in Figure 3(d), the various segments of the void phase are shown with different colors.

After each moisture-conditioning phase, the micromechanical FE meshes, with material characteristics updated for moisture damage, were subjected to displacement controlled loading. The prescribed displacement is applied diametrically across the circular cross section of the cylindrical specimen with a constant rate of 50 mm/min, replicating the loading conditions during an Indirect Tension Test (ITT).

In these simulations, viscoelastic material properties were defined for the asphalt binder. An instantaneous modulus of 3.5 MPa was specified for the purely elastic component. For the viscoelastic component, an elastic modulus of 550 MPa and a viscosity of 2200 MPa·s were specified. The mechanical properties of the aggregates were selected based on a study by Artamendi et al. *(23)*. An elastic modulus of 18.1 GPa and a Poisson's ratio of 0.171 were specified for the aggregate phase.

Figures 6 and 7 demonstrate the effect of moisture conditioning on the cohesive binder damage for the PA and the SMA mixture, respectively. Specifically, Figures 6(a) and 7(a) show the PA and SMA specimens FE mesh in dry conditions, i.e. before any moisture conditioning; for both specimens, aggregates are in yellow, asphalt binder in red and air voids in blue color. In Figures 6(d) and 7(d) the damage distribution due to mechanical loading is presented for the porous and the dense mixture, when tested in dry conditions. As expected, damage is developing along the diameter of both specimens in the direction of loading.

As moisture conditioning progresses, the results demonstrate the strong relationship between the amount of moisture content in the material and the overall level of damage development in the AC specimens. Figures 6(b-c) show the spatial distribution of moisture in the PA specimen after 48 hours and 120 hours of moisture diffusion, while Figures 6(e-f) show the internal damage distribution in the moisture weakened specimen after mechanical loading is applied.

For the SMA specimen, Figures 7(b-c) show the concentration of moisture within the body of the specimen in 48 and 120 hours, whereas Figures 7(e-f) the corresponding distribution of damage. Apparently, damage concentrates on those areas in the specimen that have their mechanical properties degraded already by moisture.

The effect of moisture conditioning on the specimen strength for both mixtures is depicted in Figures 8 and 9. As expected, the SMA mixture exhibited higher dry ITT values than the PA did, since the presence of high air voids content decreases the loading capacity of the AC specimen.

Both the PA and the SMA specimens showed gradual degradation of their mechanical strength as moisture diffusion progressed with time. The PA specimen had an overall strength reduction of 43% after 240 hrs (10 days) of moisture conditioning, while for the SMA mixture the reduction was 21%. Furthermore, the rate of degradation after 48 hours of diffusion is higher for the PA mixture.

The simulations indicate that for PA mixtures, in which the air voids content is high and pore connectivity can reach 90%, the choice of mixture components less susceptible to moisture damage is of paramount importance. In Figure 8, it can be seen that the PA specimen susceptibility to moisture damage diminishes from 43% to 18.5% with the use of a less moisture sensitive binder (moisture susceptibility parameter $\alpha_2 < \alpha_1$).

CONCLUSIONS

The CAPA-3D results indicate the importance of treating asphalt concrete as a three-phase medium in micromechanical finite element simulations and confirm the well-known facts that because moisture diffuses faster in the air voids phase, asphalt mixtures with high air voids content are more susceptible to moisture damage. The results also show that for porous mixtures in which air voids are significantly interconnected, binders with enhanced properties against moisture damage should be preferred.

Availability of the model enables evaluation and ranking of the contribution and the importance of the physico-chemical and mechanical characteristics of mastics on the moisture resistance of various types of asphalt mixes subjected to combinations of mechanical loading and moisture.

ACKNOWLEDGEMENTS

The authors gratefully acknowledge the Dutch Ministry of Transport, Public Works and Water Management and the UK Engineering and Physical Sciences Research Council for funding this project.

REFERENCES

1. Kiggundu, B.M. and F.L. Roberts. *Stripping in HMA mixtures: state-of-the-art and critical review of test methods.* NCAT Report 88-02, National Center for Asphalt Technology Alabama: Auburn University, 1988.
2. Kringos, N. and A. Scarpas. Raveling of Asphaltic Mixes Due to Water Damage: Computational Identification of Controlling Parameters. In *Transportation Research Record: Journal of the Transportation Research Board*, No. 1929, Transportation Research Board of the National Academies, Washington, D.C., 2005, pp.79–87.
3. Kringos, N., A. Scarpas, C. Kasbergen and P. Selvadurai. Modelling of Combined Physical Mechanical Moisture-Induced Damage in Asphaltic Mixes, Part 1: Governing Processes and Formulations. *International Journal of Pavement Engineering*, Vol. 9, No. 2, 2008, pp. 115-118.
4. Cheng D., D.N. Little, R.L. Lytton and J.C. Holste. Moisture Damage Evaluation of Asphalt Mixtures by Considering Both Moisture Diffusion and Repeated-Load Conditions. In *Transportation Research Record: Journal of the Transportation Research Board*, No. 1832, Transportation Research Board of the National Academies, Washington, D.C., 2003, pp. 42-49.
5. Lytton, R.L., E.A. Masad, C. Zollinger, R. Bulut and D.N. Little. *Measurements of surface energy and its relationship to moisture damage.* Technical Report No. FHWA/TX-05/0-4524-2, FHWA, Washington D.C., 2005.
6. Labib, M.E. Asphalt-aggregate Interactions and Mechanisms for Water Stripping. *Preprint American Chemical Society Division of Fuel Chemistry*, Volume 37, 1992, pp. 1472-1481.
7. Hefer, A. *Adhesion in bitumen-aggregate systems and quantification of the effects of water on the adhesive bond.* PhD dissertation. Texas A&M University, College Station, Texas, 2004.
8. Adamson, A.W. *Physical Chemistry of Surfaces.* John Wiley & Sons, Inc., New York, 1982.
9. Kringos, N., A. Scarpas, A. Copeland and J. Youtcheff. Modelling of Combined Physical Mechanical Moisture-Induced Damage in Asphaltic Mixes, Part 2: Moisture Susceptible Parameters. *International Journal of Pavement Engineering*, Vol. 9, No. 2, 2008, pp. 129-151.
10. Kringos, N. and Scarpas, A. Physical and Mechanical Moisture Susceptibility of Asphaltic Mixtures. *International Journal of Solids and Structures*, Vol. 45, No. 9, 2008, pp. 2671-2685.
11. Caro, S., E.A. Masad, A. Bhasin and D.N. Little. Micromechanical Modeling of the Influence of Material Properties on Moisture-Induced Damage in Asphalt Mixtures. *Construction and building materials*, Vol. 24, 2010, pp. 1184-1192.
12. Kim, Y.R., D.H. Allen and D.N. Little. Damage-Induced Modeling of Asphalt Mixtures Through Computational Micromechanics and Cohesive Zone Fracture. *Journal of Materials in Civil Engineering*, Vol.17, No. 5, 2005, pp. 477-484.
13. Shakiba, M., R.K. Abu Al-Rub, M.K. Darabi, T. You, E.A. Masad and D.N. Little. A Continuum Coupled Moisture-Mechanical Damage Model for Asphalt Concrete. Presented at 92nd Annual Meeting of the Transportation Research Board, Washington, D.C., 2012.
14. Kassem, E., E. Masad, R. Lytton and A. Chowdhury. Influence of Air Voids on Mechanical Properties of Asphalt Mixtures. *Road Materials and Pavement Design*, Vol. 12, No. 3, 2011, pp. 493-524.
15. Kassem, E., E. Masad, R. Lytton, and R. Bulut. Measurements of the Moisture Diffusion Coefficient of Asphalt Mixtures and its Relationship to Mixture Composition. *International Journal of Pavement Engineering*, Vol. 10, No. 6, 2009, pp. 389-399.
16. Arambula, E., E. Masad, and A. Martin. Influence of Air Void Distribution on the Moisture Susceptibility of Asphalt Mixes, *Journal of Materials in Civil Engineering*, Vol. 19, No. 8, 2007, pp. 655–664.

17. Masad, E., A. Castelblanco and B. Birgisson. Effects of Air Void Size Distribution, Pore Pressure, and Bond Energy on Moisture Damage. *Journal of Testing and Evaluation*, Vol. 34, No.1, 2006.
18. Scarpas, A. *CAPA-3D: A mechanics based computational platform for pavement engineering*, PhD dissertation. Delft University of Technology, Netherlands, 2005.
19. Coleman, B.D. and M. Gurtin. Thermodynamics with Internal Variables. *Journal of Chemical Physics*, Vol. 47, 1967.
20. Kringos, N., R. Khedoe, A. Scarpas, and A. de Bondt. New Asphalt Concrete Moisture Susceptibility Test Methodology. Presented at 90th Annual Meeting of the Transportation Research Board, Washington, D.C., 2011.
21. *Simpleware*, ScanIP, +ScanFE, 2011.
22. Kringos, N., A. Scarpas, and A. de Bondt. Determination of Moisture Susceptibility of Mastic-Stone Bond Strength and Comparison to Thermodynamical Properties. *Journal of the Association of Asphalt Paving Technologists*, Vol. 77, 2008, pp. 435-478.
23. Artamendi, I., M. Kane, A. Scarpas and M.M. Villani. *Measurement of the interface component characteristics*. EU FP7 SKIDSAFE project report 1.1, 2011.

LIST OF TABLES

LIST OF FIGURES

TABLE 1 Aggregate Gradation

Sieve size (mm)		14	10	6.3	4	2	1	0.063
Passing (%)	**SMA**	100	90	47	29	25	21	10.1
	PA	100	99	47	27	19	14	5.6

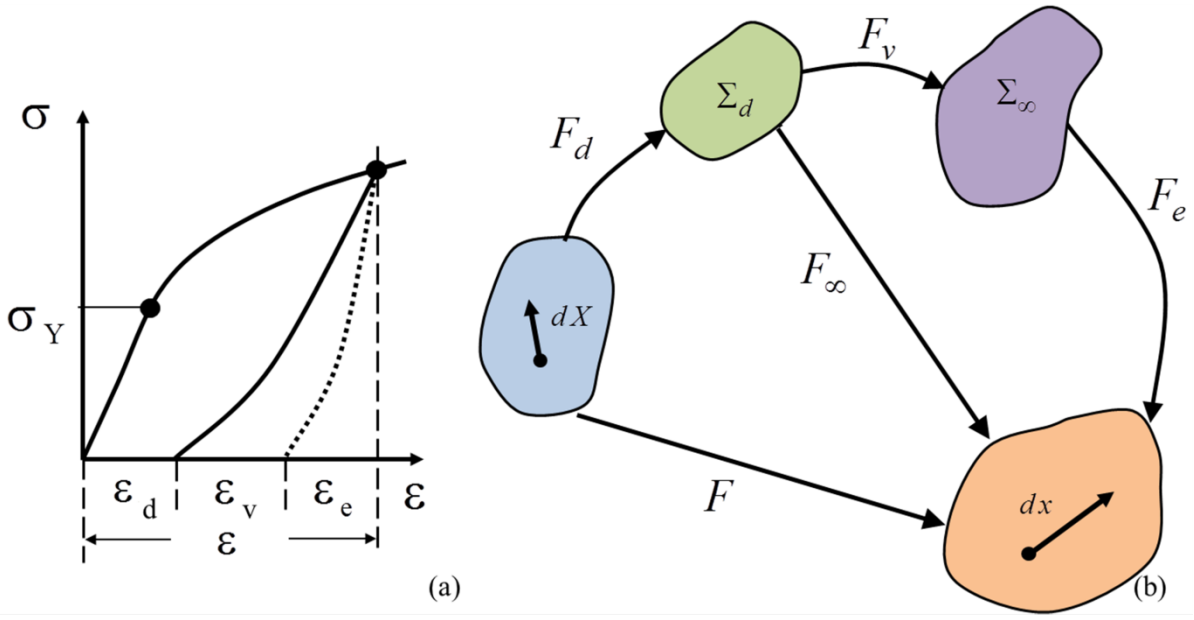

FIGURE 1 (a) Schematic of viscoelastic- damage model response (σ is the stress; σ_Y is the yield stress; $\varepsilon=\varepsilon_d+\varepsilon_v+\varepsilon_e$, where ε is the total strain, ε_d is the strain due to damage, ε_v is the viscous strain and ε_e is the elastic strain; (b) Multiplicative decomposition of the deformation gradient tensor.

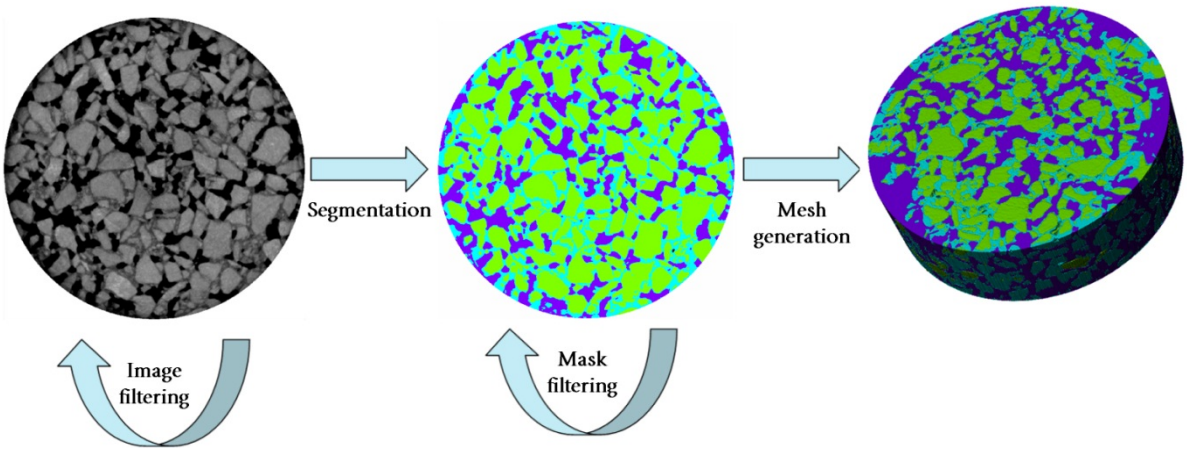

FIGURE 2 Process flow for the development of the FE meshes.

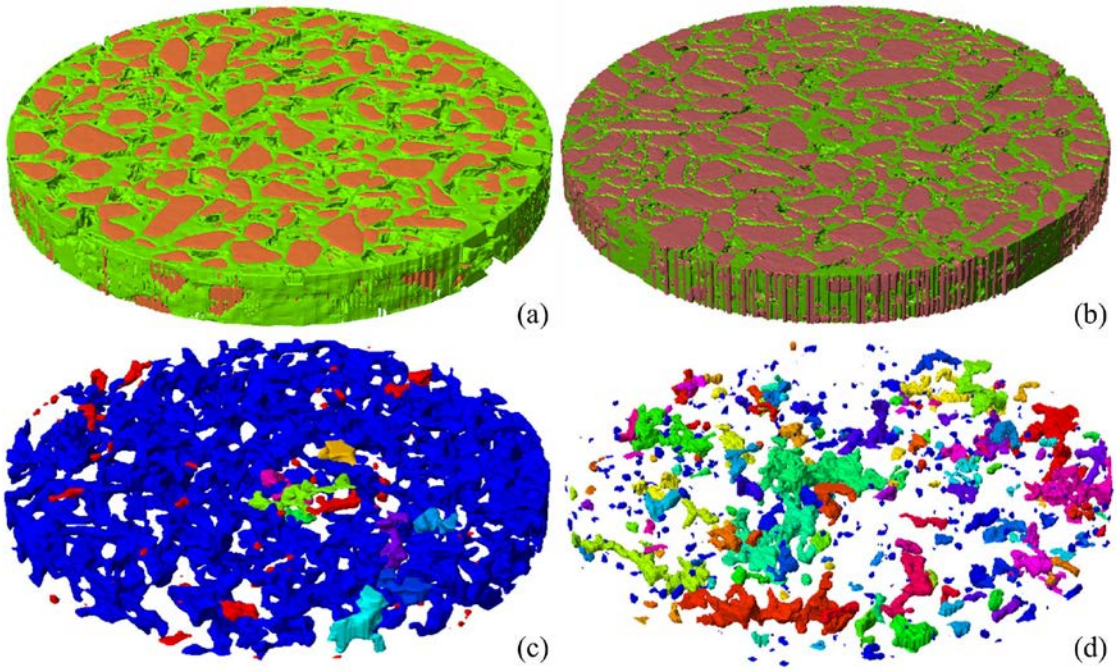

FIGURE 3 Volume renderings of the FE mesh (a) and the air void phase (c) for the PA mixture; FE mesh (b) and air void phase (d) for the SMA mixture.

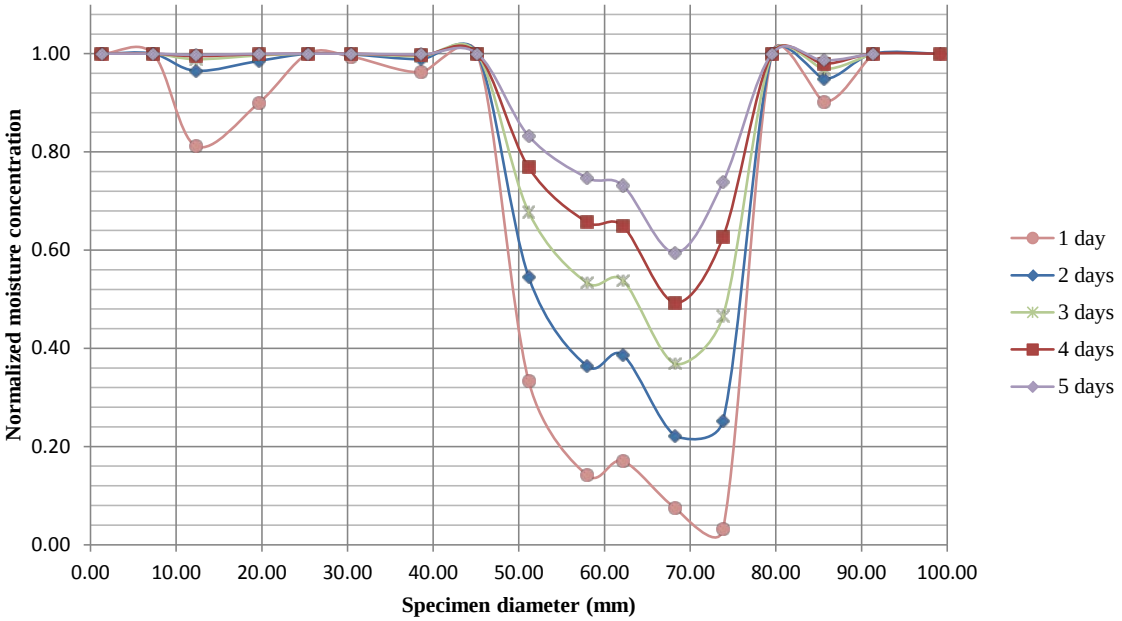

FIGURE 4 Moisture concentration profile within the PA specimen at different time intervals.

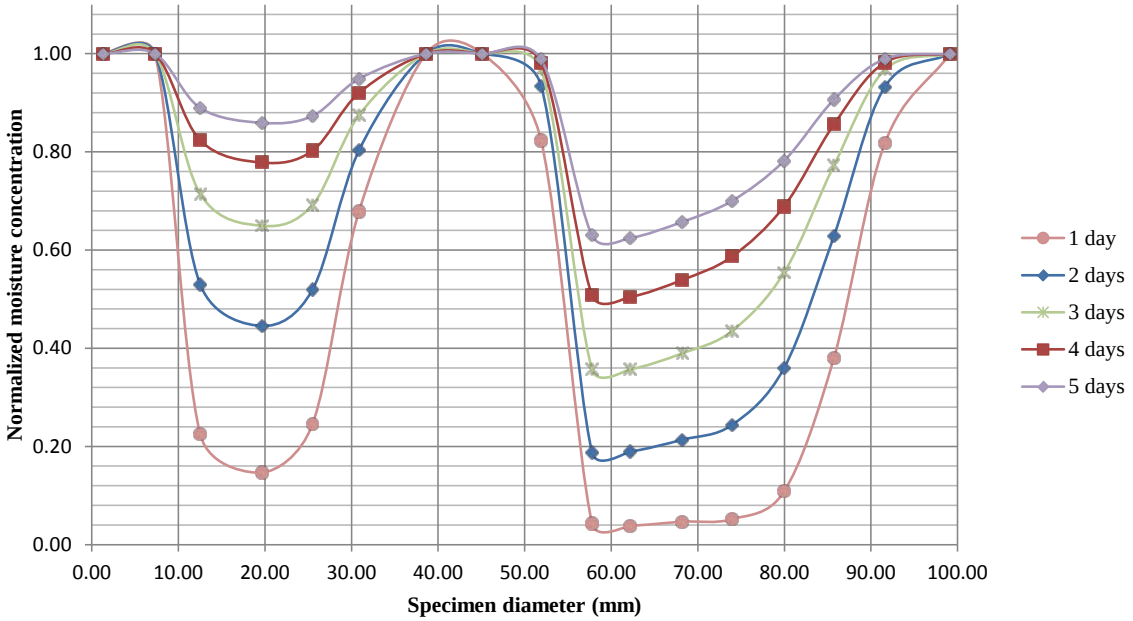

FIGURE 5 Moisture concentration profile within the SMA specimen at different time intervals.

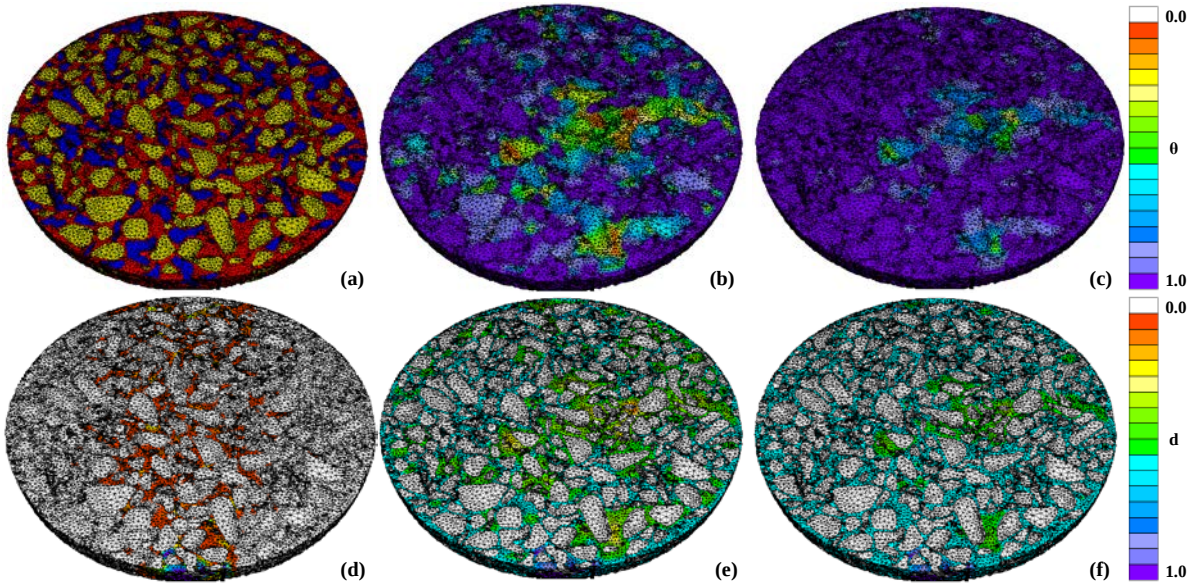

FIGURE 6 Moisture concentration and damage distribution in the PA specimen after 0 hours (a, d), 48 hours (b, e) and 120 (c, f) hours of moisture diffusion.

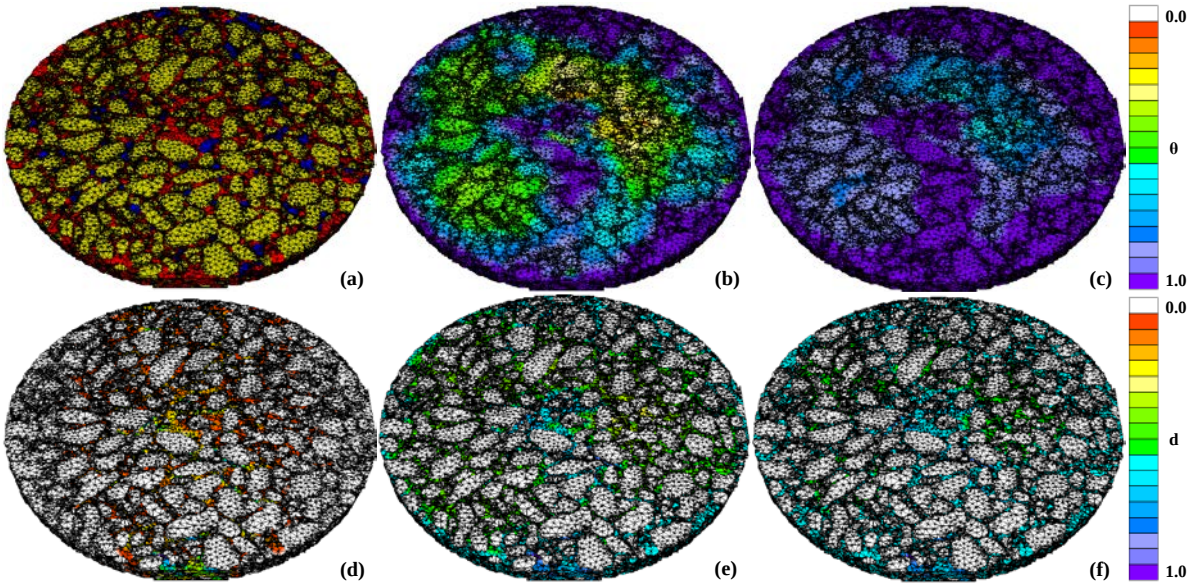

FIGURE 7 Moisture concentration and damage distribution in the SMA specimen after 0 hours (a, d), 48 hours (b, e) and 120 hours (c, f) of moisture diffusion.

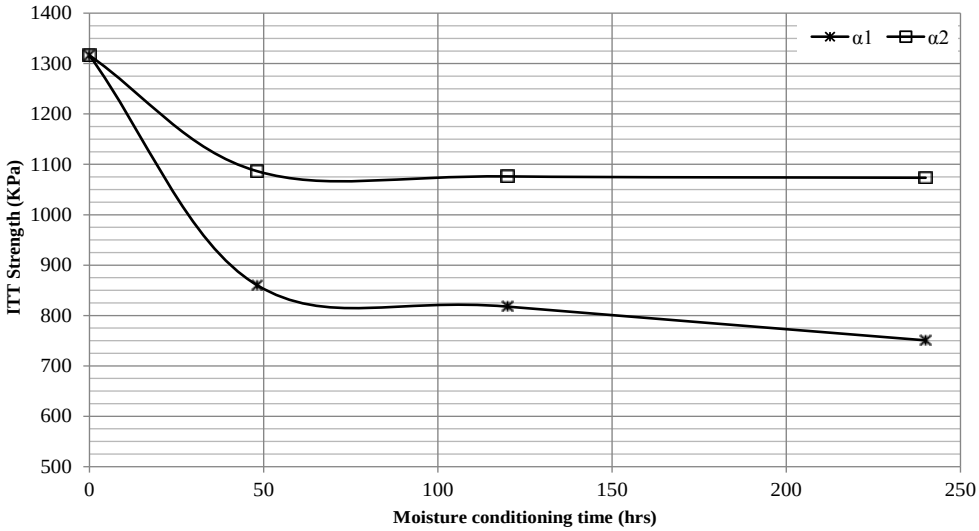

FIGURE 8 Influence of moisture conditioning time on ITT strength for the PA mixture.

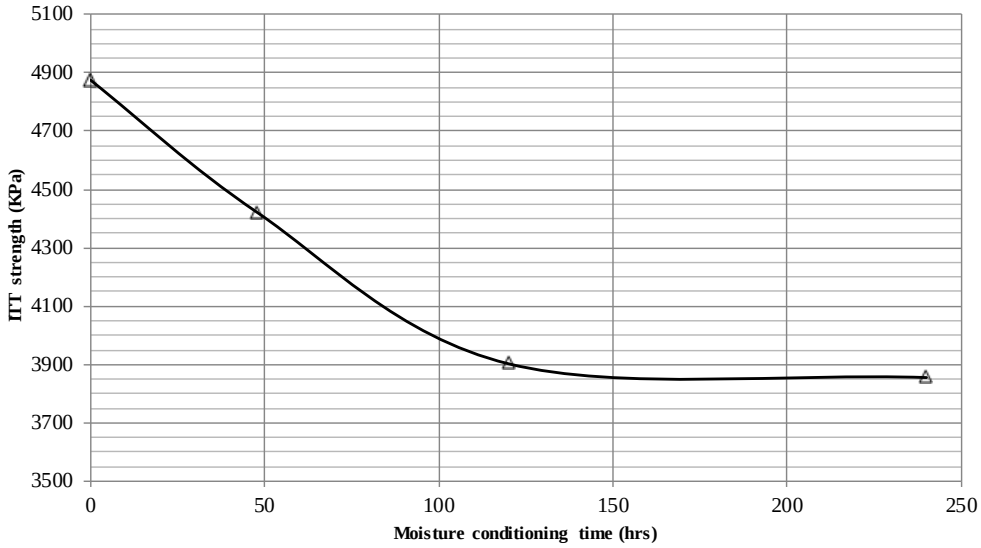

FIGURE 9 Influence of moisture conditioning time on ITT strength for the SMA mixture.